(Preprint) AAS 15-758

NAVIGATION AND DISPERSION ANALYSIS OF THE FIRST ORION EXPLORATION MISSION

Renato Zanetti*, and Christopher D'Souza†

This paper seeks to present the Orion EM-1 Linear Covariance Analysis for the DRO mission. The $|\Delta V|$ statistics for each maneuver are presented. Included in the memo are several sensitivity analyses: variation in the time of OTC-1 (the first outbound correction maneuver), variation in the accuracy of the trans-Lunar injection, and variation in the length of the optical navigation passes.

INTRODUCTION

This memo seeks to document the navigation and dispersion analysis for the Orion EM-1 Distant Retrograde Orbit (DRO) mission. It is based upon the theory presented in Maybeck.[1] This is a further analysis of the DRO trajectory along the lines of what was presented by D'Souza and Zanetti.[2]

The accuracy of the flight-path angle at EI is driven by several factors including the navigation, targeting, and burn execution errors at the time of the last mid-course maneuver, and unaccounted trajectory perturbations between the last mid-course maneuver and EI. Apollo missions tolerated a maximum flight path angle error at EI of ± 1 degree, with half of this error allocated to navigation. A similar criterion is employed in this study.

Perturbations are a major source of errors in the cislunar navigation performance of Orion. In a perfect world all the sources of perturbations would be modeled in the filter dynamics. However, computational limitations preclude such extensive modeling. Therefore, the primary sources of perturbations are characterized. In particular there are three categories of unmodeled acceleration: propulsive sources, gravitational perturbations, and solar radiation pressure. Only propulsive errors are included in this analysis; the gravitational and solar radiation pressure are not included – they will be included in a future study. For EM1, the gravitational and solar radiation pressure errors are several orders of magnitude below the thrusting sources. The propulsive sources considered are: attitude deadbands, attitude slews, CO_2 venting, and sublimator venting.

Linear covariance techniques are used to perform the analysis for the Orion Cislunar missions. This comports well for the navigation system design since the cislunar navigation system on Orion will be an Extended Kalman Filter. Many of the same states and dynamics used in the linear covariance analysis will be used in the on-board cislunar navigation system. A preliminary design of the cislunar navigation system is presented. This is supported by linear covariance analyses which provides navigation performance, trajectory dispersion performance and $|\Delta \mathbf{V}|$ usage.

*Aerospace Engineer, EG6, NASA/JSC, Houston, TX.
†Aerospace Engineer, EG6, NASA/JSC, Houston, TX.

The paper is organized as follows: Section 2 will contain a brief description of linear covariance analysis. In Section 3, the navigation system will be described, both the filter dynamics as well as the measurement. Section 4 will contain results of this analysis. Section 5 contains the sensitivity analysis when the time of OTC-1 is varied. Section 6 contains the sensitivity analysis when the accuracy of the Trans-Lunar Injection (TLI) is varied. Section 7 contains the sensitivity analysis when the length of the optical navigation pass is varied. Finally, a few concluding comments are made in Section 8.

LINEAR COVARIANCE ANALYSIS

This investigation is performed using linear covariance (LinCov) analysis techniques.[?,3] The state vector is taken to be

$$\mathbf{x} = \begin{Bmatrix} \mathbf{r}^{\mathrm{T}} & \mathbf{v}^{\mathrm{T}} & \boldsymbol{\theta}^{\mathrm{T}} & \mathbf{m}_{op}^{\mathrm{T}} & \mathbf{m}_{tr}^{\mathrm{T}} & \mathbf{b}_{cent}^{\mathrm{T}} & b_{pd} \end{Bmatrix}^{\mathrm{T}}. \tag{1}$$

LINEAR COVARIANCE ANALYSIS

This investigation is performed using linear covariance (LinCov) analysis techniques.[?,3] The state vector is taken to be

$$\mathbf{x} = \begin{Bmatrix} \mathbf{r}^{\mathrm{T}} & \mathbf{v}^{\mathrm{T}} & \boldsymbol{\theta}^{\mathrm{T}} & \mathbf{m}_{op}^{\mathrm{T}} & \mathbf{m}_{tr}^{\mathrm{T}} & \mathbf{b}_{cent}^{\mathrm{T}} & b_{pd} \end{Bmatrix}^{\mathrm{T}}. \tag{2}$$

where $\mathbf{r}$ is the position of the vehicle with respect to the primary body, $\mathbf{v}$ is the corresponding velocity with respect to the primary, $\boldsymbol{\theta}$ is the attitude error, $\mathbf{m}_{op}$ is teh misalignment of the optical instrument, $\mathbf{b}_{tr}$ is the bias position of the instrument with respect to the navigation base, $\mathbf{b}_{cent}$ is the bias of the planetary centroid measurement, and b_{pd} is the bias of the planetary diameter measurement.

The nominal trajectory is obtained by integrating the nominal dynamics model with an Encke-Nystrom method.[?] Neither the rotation vector $\boldsymbol{\theta}$ nor its uncertainty are integrated in this analysis. The nominal attitude is known at any time and it does not need to be calculated. The attitude estimation error covariance is constant and is driven by the star tracker accuracy. The attitude navigation dispersion covariance is constant and is given by the attitude control dead-band. The attitude environment dispersion covariance is constant and obtained from the above two quantities assumed uncorrelated. Before the star elevation is determined, the vehicle slews in preparation for measurement acquisition. This attitude maneuver is performed by the onboard thrusters and is assumed to be instantaneous. Due to thruster misalignment, this maneuver adds uncertainty to the translational states. After the batch of measurements is available, the vehicle returns to its nominal attitude. In linear covariance analysis, the difference between the true state and the nominal state is defined as the environment dispersion

$$\delta\mathbf{x} \triangleq \mathbf{x} - \bar{\mathbf{x}}. \tag{3}$$

The difference between the estimated state and the nominal state is defined as the navigation dispersion

$$\delta\hat{\mathbf{x}} \triangleq \hat{\mathbf{x}} - \bar{\mathbf{x}}. \tag{4}$$

Finally, the difference between the true state and the estimated state, is defined as the estimation error, sometimes referred to as the onboard navigation error

$$\mathbf{e} \triangleq \mathbf{x} - \hat{\mathbf{x}}. \tag{5}$$

Following the standard Kalman filter assumptions, the difference between the nominal and estimated models is represented with zero-mean, white noise. The estimated state evolves as

$$\dot{\hat{\mathbf{x}}} = \mathbf{f}(\hat{\mathbf{x}}), \tag{6}$$

where $\mathbf{f}$ is a nonlinear function representing the system dynamics as modeled by the filter. The evolution of the nominal state is modeled as

$$\dot{\bar{\mathbf{x}}} = \bar{\mathbf{f}}(\bar{\mathbf{x}}) = \mathbf{f}(\bar{\mathbf{x}}) + \boldsymbol{\upsilon}, \tag{7}$$

where $\bar{\mathbf{f}}$ is a nonlinear function representing the state dynamics as modeled in designing the nominal trajectory. The nominal dynamics $\bar{\mathbf{f}}$ may be higher fidelity than the filter's dynamics $\mathbf{f}$. The vector $\boldsymbol{\upsilon}$ represents the dynamics modeled in the nominal trajectory but neglected in the filter models. In Kalman filtering, the difference between the true dynamics and the filter's dynamics is called process noise. While these unmodeled dynamics are not actually white noise, they are modeled as such. The power spectral density of process noise is then tuned to achieve good performance. The same procedure is used here. In order to capture the difference between the two dynamical models, $\boldsymbol{\upsilon}$ is modeled as a zero-mean white process with spectral density $\hat{\mathbf{Q}}$. The goal is to represent the increased value of the navigation dispersion during propagation due to the difference between the nominal and filter's dynamical models.

The evolution of the navigation dispersion can be approximated to first-order as

$$\delta\dot{\hat{\mathbf{x}}} = \dot{\hat{\mathbf{x}}} - \dot{\bar{\mathbf{x}}} = \mathbf{f}(\bar{\mathbf{x}} + \delta\hat{\mathbf{x}}) - \mathbf{f}(\bar{\mathbf{x}}) - \boldsymbol{\upsilon} \simeq \mathbf{F}(\bar{\mathbf{x}})\delta\hat{\mathbf{x}} - \boldsymbol{\upsilon}. \tag{8}$$

The evolution of the navigation dispersion covariance is governed by

$$\dot{\hat{\mathbf{P}}} = \mathbf{F}(\bar{\mathbf{x}})\hat{\mathbf{P}} + \hat{\mathbf{P}}\mathbf{F}(\bar{\mathbf{x}})^{\mathrm{T}} + \hat{\mathbf{Q}}. \tag{9}$$

Similarly, the true state is modeled to evolve as

$$\dot{\mathbf{x}} = \mathbf{f}(\mathbf{x}) + \boldsymbol{\nu}. \tag{10}$$

The evolution of the estimation error is given by

$$\dot{\mathbf{e}} = \dot{\mathbf{x}} - \dot{\hat{\mathbf{x}}} \simeq \mathbf{f}(\bar{\mathbf{x}}) + \mathbf{F}(\bar{\mathbf{x}})(\mathbf{x} - \bar{\mathbf{x}}) + \boldsymbol{\nu} - \mathbf{f}(\bar{\mathbf{x}}) - \mathbf{F}(\bar{\mathbf{x}})(\hat{\mathbf{x}} - \bar{\mathbf{x}}) = \mathbf{F}(\bar{\mathbf{x}})\mathbf{e} + \boldsymbol{\nu}. \tag{11}$$

Vector $\boldsymbol{\nu}$ is modeled as zero mean white noise with spectral density $\mathbf{Q}$. The onboard covariance $\mathbf{P}$ evolves as

$$\dot{\mathbf{P}} = \mathbf{F}(\bar{\mathbf{x}})\mathbf{P} + \mathbf{P}\mathbf{F}(\bar{\mathbf{x}}) + \mathbf{Q}. \tag{12}$$

Notice that the Jacobian $\mathbf{F}$ could be evaluated at the estimated state $\hat{\mathbf{x}}$ instead of the nominal state $\bar{\mathbf{x}}$, as in the extended Kalman filter.

Finally

$$\delta\dot{\mathbf{x}} = \dot{\mathbf{x}} - \dot{\bar{\mathbf{x}}} \simeq \mathbf{F}(\bar{\mathbf{x}})\delta\mathbf{x} + \boldsymbol{\nu} - \boldsymbol{\upsilon} \tag{13}$$

and $\bar{\mathbf{P}}$ evolves as

$$\dot{\bar{\mathbf{P}}} = \mathbf{F}(\bar{\mathbf{x}})\bar{\mathbf{P}} + \bar{\mathbf{P}}\mathbf{F}(\bar{\mathbf{x}}) + \bar{\mathbf{Q}}. \tag{14}$$

Notice that $\bar{\mathbf{Q}} = \mathbf{Q} + \hat{\mathbf{Q}}$ if $\boldsymbol{\nu}$ and $\boldsymbol{\upsilon}$ are assumed to be uncorrelated.

THE ORION CISLUNAR NAVIGATION FILTER

The Filter Dynamics

Since this filter operates once Orion is away from Earth (and outside of GPS range), the primary forces governing the motion of the vehicle are the gravitational forces of the Earth, the Moon, and the Sun. The trajectory is designed taking into account all three of these bodies. Whereas the equations of motion are formulated with respect to a central body, this (central body) changes depending on which sphere of influence the vehicle is subject to.

The equations of motion for the Earth-Sun-Moon system are

$$\ddot{\mathbf{r}}_{PV} = -\frac{\mu_P}{r_{PV}^3}\mathbf{r}_{PV} - \mu_Q\left[\frac{\mathbf{r}_{QV}}{r_{QV}^3} + \frac{\mathbf{r}_{PQ}}{r_{PQ}^3}\right] - \mu_S\left[\frac{\mathbf{r}_{SV}}{r_{SV}^3} + \frac{\mathbf{r}_{PS}}{r_{PS}^3}\right] \tag{15}$$

where and $\mathbf{r}_{PV}$ is the position of the vehicle (V) with respect to the primary body (P), $\mathbf{r}_{QV}$ is the position of the vehicle with respect to the secondary body (Q), $\mathbf{r}_{PQ}$ is the position of the secondary body with respect to the primary body, $\mathbf{r}_{SV}$ is the position of the vehicle with respect to the Sun (S), and $\mathbf{r}_{PS}$ is the position of the Sun with respect to the primary body. The geometry is shown in Figure 2. In many applications, these equations are integrated by a Runge-Kutta or Runge-Kutta-Fehlberg fixed-step or variable-step algorithms.

However, blindly applying a standard fourth-order Runge-Kutta method can lead to numerical errors (if large step sizes are taken) not to mention inefficiencies (if small step sizes are taken). The Encke-Nyström method has been shown to have none of these deficiencies – large step sizes can be taken and numerical precision maintained at the same time.

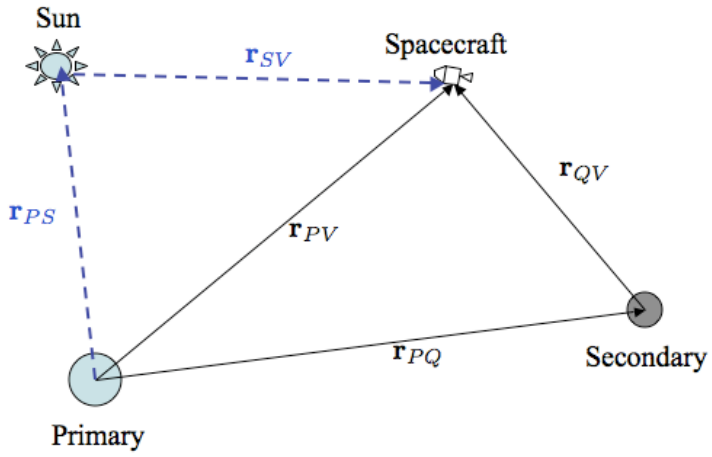

Figure 1. The Earth-Sun-Moon-Vehicle Geometry

The Encke-Nyström Method The Encke-Nyström method has an illustrious legacy. Unlike the Cowell's method, only the perturbations away from two-body motion are integrated. As such, the perturbations being integrated are small and excellent numerical precision is retained. In addition, since the force-field under which the equations of motion being integrated is conservative, and since the velocity derivatives are expressed in terms of the position only, a Nyström formulation of integration is used. The disadvantage of this method is that there is a bit of mathematical set-up required. However, if one is willing to pay this price, the dividends are enormous – both in terms of precision and computation time. The equations which are integrated are as follows:

$$\ddot{\mathbf{r}}_{PV} = -\frac{\mu_P}{r_{PV}^3}\mathbf{r}_{PV} - \frac{\mu_Q}{r_{QV}^3}\left[f(q_Q)\mathbf{r}_{PQ} + \mathbf{r}_{PV}\right] - \frac{\mu_S}{r_{SV}^3}\left[f(q_S)\mathbf{r}_{PS} + \mathbf{r}_{PV}\right] \tag{16}$$

where

$$\begin{aligned} q_{(\,)} &= \frac{\left(\mathbf{r}_{PV} - 2\mathbf{r}_{P(\,)}\right)\cdot \mathbf{r}_{PV}}{r_{P(\,)}^2} \\ f(q_{(\,)}) &= q_{(\,)}\frac{3 + 3q_{(\,)} + q_{(\,)}^2}{1 + \left(1 + q_{(\,)}\right)^{3/2}} \end{aligned}$$

This formulation was used in the Apollo program.[?] It should be noted that Eqs.(15) and (16) are mathematically equivalent.

In order to compute the state transition matrix from an epoch to another epoch in the future (or the past), the partial of the future (or past) state with respect to the initial epoch must be computed. The reason the Encke-Nyström algorithm is introduced into this discussion is that the Encke-Nyström method is predicated on "small" deviations from a reference (osculating) orbit. This is precisely the foundation upon which the state transition matrix for the cislunar trajectory is built and it is also the foundation upon which linear covariance analysis is built. Whereas the state transition matrix is defined as

$$\begin{aligned} \Phi(t, t_0) &= \left(\frac{\partial \mathbf{X}(t)}{\partial \mathbf{X}(t_0)}\right)_{\mathbf{X}_{nom}} \\ &= \left[\begin{array}{cc} \frac{\partial \mathbf{r}}{\partial \mathbf{r}_0} & \frac{\partial \mathbf{r}}{\partial \mathbf{v}_0} \\ \frac{\partial \mathbf{v}}{\partial \mathbf{r}_0} & \frac{\partial \mathbf{v}}{\partial \mathbf{v}_0} \end{array}\right]_{\mathbf{X}_{nom}} \end{aligned}$$

the partials of the dynamics are defined as

$$\mathbf{A}(t) = \left(\frac{\partial \dot{\mathbf{X}}}{\partial \mathbf{X}}\right)_{\mathbf{X}_{nom}}(t).$$

With the dynamics defined in Eq. (40), the partials of the dynamics are found to be

$$\mathbf{A}(t) = \left[\begin{array}{cc} \mathbf{0}_{3\times 3} & \mathbf{I}_3 \\ \mathbf{G}(t) & \mathbf{0}_{3\times 3} \end{array}\right] \tag{17}$$

where $\mathbf{G}(t)$ is defined as

$$\begin{aligned}\mathbf{G}(t) &= -\frac{\mu_P}{r_{PV}^3}\left(I_3 - 3\frac{\mathbf{r}_{PV}\mathbf{r}_{PV}^T}{r_{PV}^2}\right) - \frac{\mu_Q}{r_{QV}^3}I_3 - \frac{\mu_S}{r_{SV}^3}I_3 + 3\mu_Q\left(f(q_Q)\mathbf{r}_{PQ} + \mathbf{r}_{PV}\right)\frac{\mathbf{r}_{QV}^T}{r_{QV}^5} \\ &\quad + 3\mu_S\left(f(q_S)\mathbf{r}_{PS} + \mathbf{r}_{PV}\right)\frac{\mathbf{r}_{SV}^T}{r_{SV}^5} - \mu_Q\frac{\mathbf{r}_{PQ}}{r_{QV}^3}\frac{\partial f(q_Q)}{\partial \mathbf{r}_{PV}} - \mu_S\frac{\mathbf{r}_{PS}}{r_{SV}^3}\frac{\partial f(q_S)}{\partial \mathbf{r}_{PV}}\end{aligned}$$

In the preceding equation, $\frac{\partial f(q_{()})}{\partial \mathbf{r}_{PV}}$ is defined as

$$\frac{\partial f(q_{()})}{\partial \mathbf{r}_{PV}} = f_{q_{()}}(q_{()})\frac{2\left(\mathbf{r}_{PV} - \mathbf{r}_{P()}\right)^T}{r_{P()}^2}$$

and

$$f_{q_{()}}(q_{()}) = \frac{[3 + 3q_{()}(2 + q_{()})](1 + (1 + q_{()})^{3/2}) - 1.5q_{()}(3 + 3q_{()} + q_{()}^2)\sqrt{q_{()} + 1}}{(1 + (1 + q_{()})^{3/2})^2}.$$

The Trajectory Partials **The Measurements**

Optical measurements were processed every 60 seconds. The optical measurements consist of star-horizon measurements and apparent angular radius measurements. These measurements take into account when the planetary disk as projected on the focal plane is both larger than and smaller than the field of view.

Planetary Centroid Measurement

In the past, the camera angles have been expressed in terms of two Euler angles, which we choose as follows, to allow for the boresight to be (nearly) along the $z-$axis, as

$$\mathbf{i}_{P/cam}^{cam} = \begin{bmatrix} \sin\alpha\cos\beta \\ \sin\beta \\ \cos\alpha\cos\beta \end{bmatrix} \tag{18}$$

so that the components of the target in camera coordinates is

$$x_{P/cam} = r\sin\alpha\cos\beta \tag{19}$$

$$y_{P/cam} = r\sin\beta \tag{20}$$

$$z_{P/cam} = r\cos\alpha\cos\beta \tag{21}$$

If instead we are interested in the coordinates in the image plane, u and v such that the vector to the point of interest is

$$\mathbf{u} = \begin{bmatrix} \frac{u_p - u}{fs_x} \\ \frac{v_p - v}{fs_y} \\ 1 \end{bmatrix} \tag{22}$$

where, as seen in Figure 2, (u_p, v_p) are the coordinates of the principal point (i.e. the point where the camera boresight intersects the image plane), s_x and s_y are the x-axis and y-axis scale factors, respectively, in units of pixels/length, and f is the focal length of the camera optics.

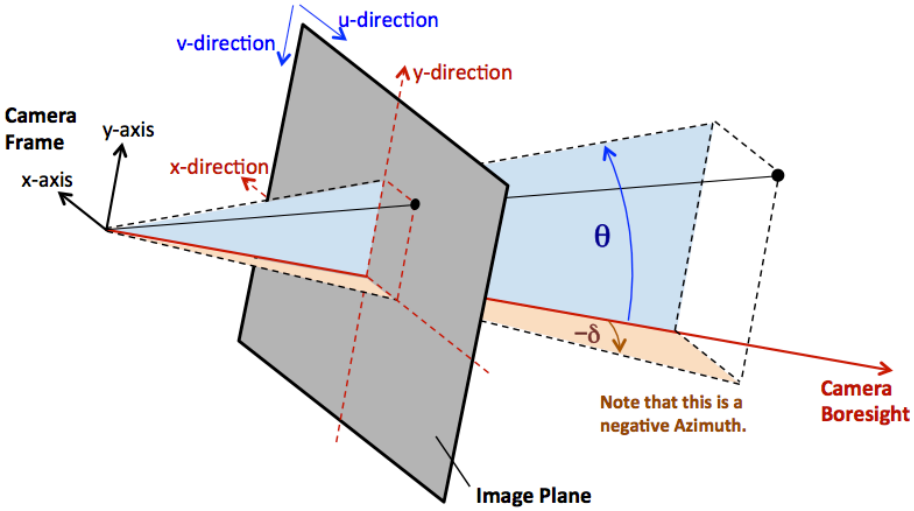

Figure 2. Camera Image Plane Coordinates

The unit vector of the line-of-sight vector can also be expressed in terms of the horizontal and vertical angles, δ and θ, where

$$\tan\delta = \frac{u_p - u}{f s_x} \tag{23}$$

$$\tan\theta = \frac{v_p - v}{f s_y} \tag{24}$$

as

$$\mathbf{i}_{P/cam}^{cam} = \frac{1}{\sqrt{\tan^2\delta + \tan^2\theta + 1}} \begin{bmatrix} \tan\delta \\ \tan\theta \\ 1 \end{bmatrix} \tag{25}$$

We can relate the two sets of coordinates[‡] as follows:

$$\tan\alpha = \tan\delta \tag{30}$$

$$\tan\beta = \tan\theta\cos\delta \tag{31}$$

[‡]We note that

$$\cos\delta = \frac{f s_x}{\sqrt{(u_p - u)^2 + f^2 s_x^2}} \tag{26}$$

$$\cos\theta = \frac{f s_y}{\sqrt{(v_p - v)^2 + f^2 s_y^2}} \tag{27}$$

$$\sin\delta = \frac{u_p - u}{\sqrt{(u_p - u)^2 + f^2 s_x^2}} \tag{28}$$

$$\sin\theta = \frac{v_p - v}{\sqrt{(v_p - v)^2 + f^2 s_y^2}} \tag{29}$$

Thus

$$\alpha = \delta \tag{32}$$

Whereas the geometry of the horizontal and vertical angles in the focal (and image) plane are useful (particularly for correcting for radial distortion), we can directly relate the u, v coordinates to the position of the planet in the camera frame as

$$\frac{u_p - u}{s_x f} = \frac{x^{cam}_{P/cam}}{z^{cam}_{P/cam}} \tag{33}$$

$$\frac{v_p - v}{s_y f} = \frac{y^{cam}_{P/cam}}{z^{cam}_{P/cam}} \tag{34}$$

where $x^{cam}_{P/cam}$, $y^{cam}_{P/cam}$ and $z^{cam}_{P/cam}$ are the Cartesian coordinates of the planet with respect to the camera expressed in camera coordinates (corresponding to $\mathbf{r}^{cam}_{P/cam}$.

Concept of Operations of Maneuvers and Optical Navigation Passes

It was assumed that there were 4 outbound trajectory correction (OTC) maneuvers on the leg from the Earth to the Moon, a single powered flyby maneuver (PFM-1) targeted for the DRO insertion point, two outbound correction maneuvers between the PFM-1 and the DRO Insertion (DRO-I) point. Once on the DRO, there were 3 (DRO) Orbit Maneuvers (OM) spaced approximately equally, all targeting the DRO Departure maneuver point. After the DRO Departure (DRO-D) Maneuver, there are two correction maneuvers targeted the perilune conditions of the second Powered flyby maneuver (PFM-2). Finally, at after PFM-2, there are three correction maneuvers. These maneuvers and their TIGs are outlined in Table 1. Note that the times of the maneuvers (TIGs) in the table are MET, with TLI occuring at an MET of 3.81 hours, so that OCT-1 occurs at TLI + 6 hours. As well the $|\Delta \mathbf{V}_{nom}|$ are the nominal size (magnitude) of the maneuver. The non-zero maneuvers (PFM-1, DOR-I, DRO-D, PFM-2) are the deterministic maneuvers and the remainder are the correction maneuvers (with a nominal size of zero).

The navigation passes were chosen so as to conclude 1 hour before each maneuver. This was to allow for the final targeting of the maneuver as well as time to perform an attitude maneuver to get to the maneuver attitude. During those epochs when the maneuvers occured more than 24 hours apart, navigation passes were scheduled so as to ensure that the onboard state remained reasonable.

TRAJECTORY AND DISPERSION ANALYSIS FOR THE EM-1 (DRO) MISSION

Table 2 contains the data for the injection covariance matrix used in this analysis. Table 3 contains the model for the process noise used during the mission, both quiescent and active.[4] Tables 4 and 5 contain the optical navigation camera parameters and error model, respectively. Finally, Table 6 contains the maneuver execution errors for this case.

The Navigation Errors for the entire trajectory are presented in Figures 3 and 4. The corresponding trajectory dispersions for the entire trajectory are presented in Figures 5 and 6. The legend "Lunar Tracking" indicates that period of time when the Moon is tracked.

Trans-DRO Phase

The navigation errors mapped to DRO Insertion errors are presented in Figures 7-8. The trajectory disperions mapped to DRO insertion trajectory dispersions are presented in Figures 9-10.

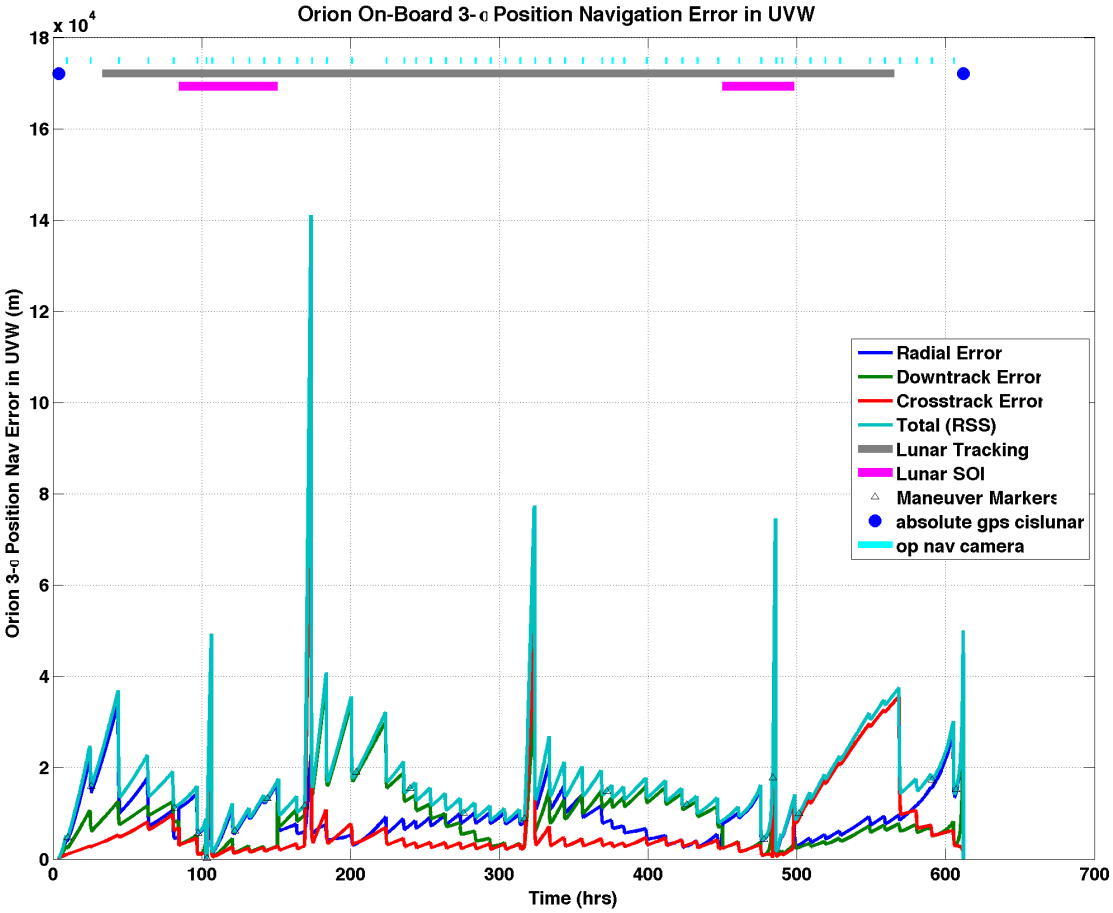

Figure 3. Onboard Position Navigation Error for the Entire Trajectory

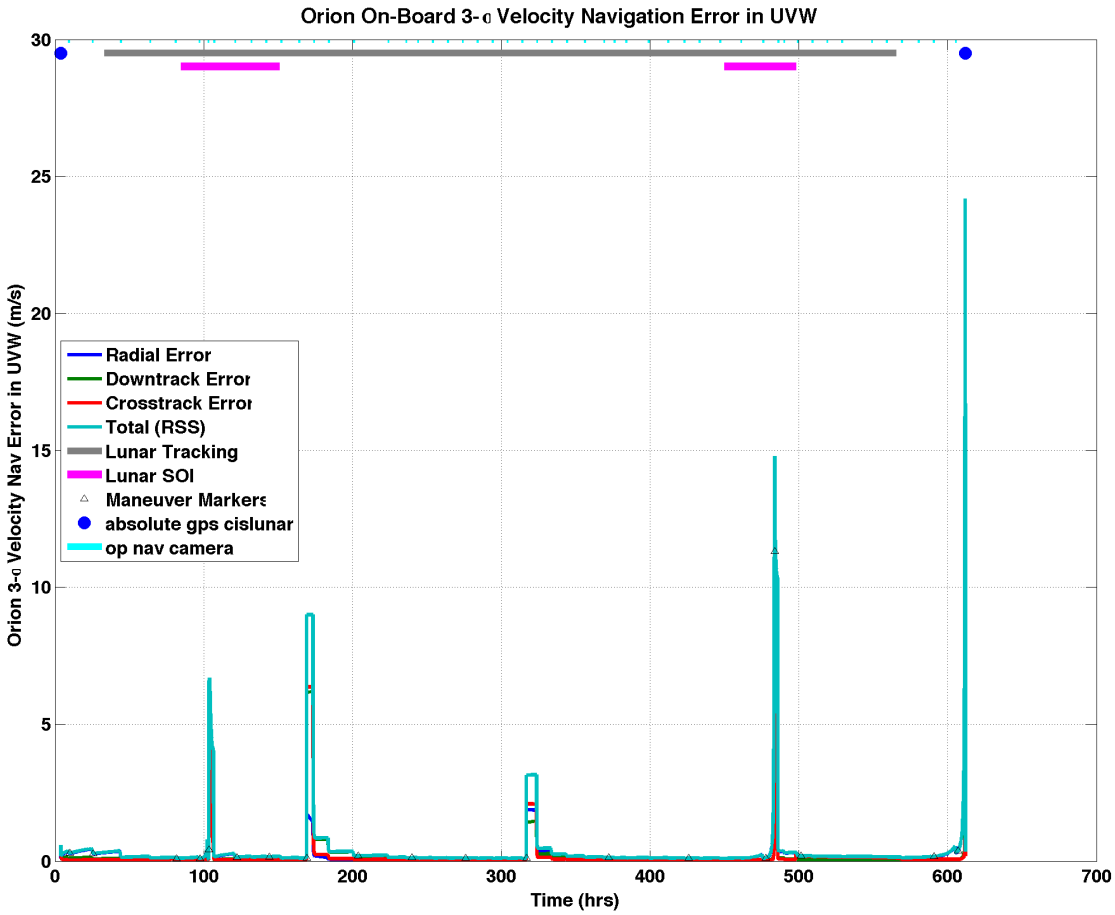

Figure 4. Onboard Velocity Navigation Error for the Entire Trajectory

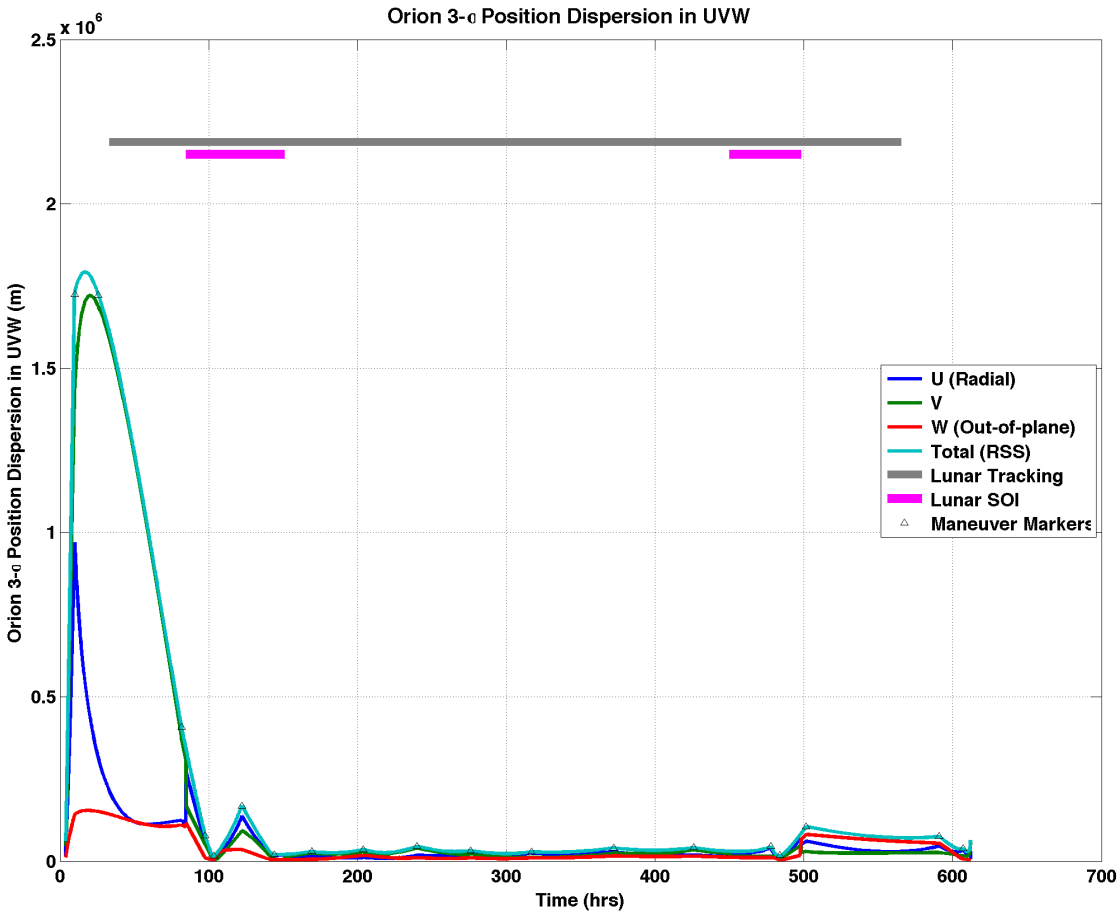

Figure 5. Position Trajectory Dispersions for the Entire Trajectory

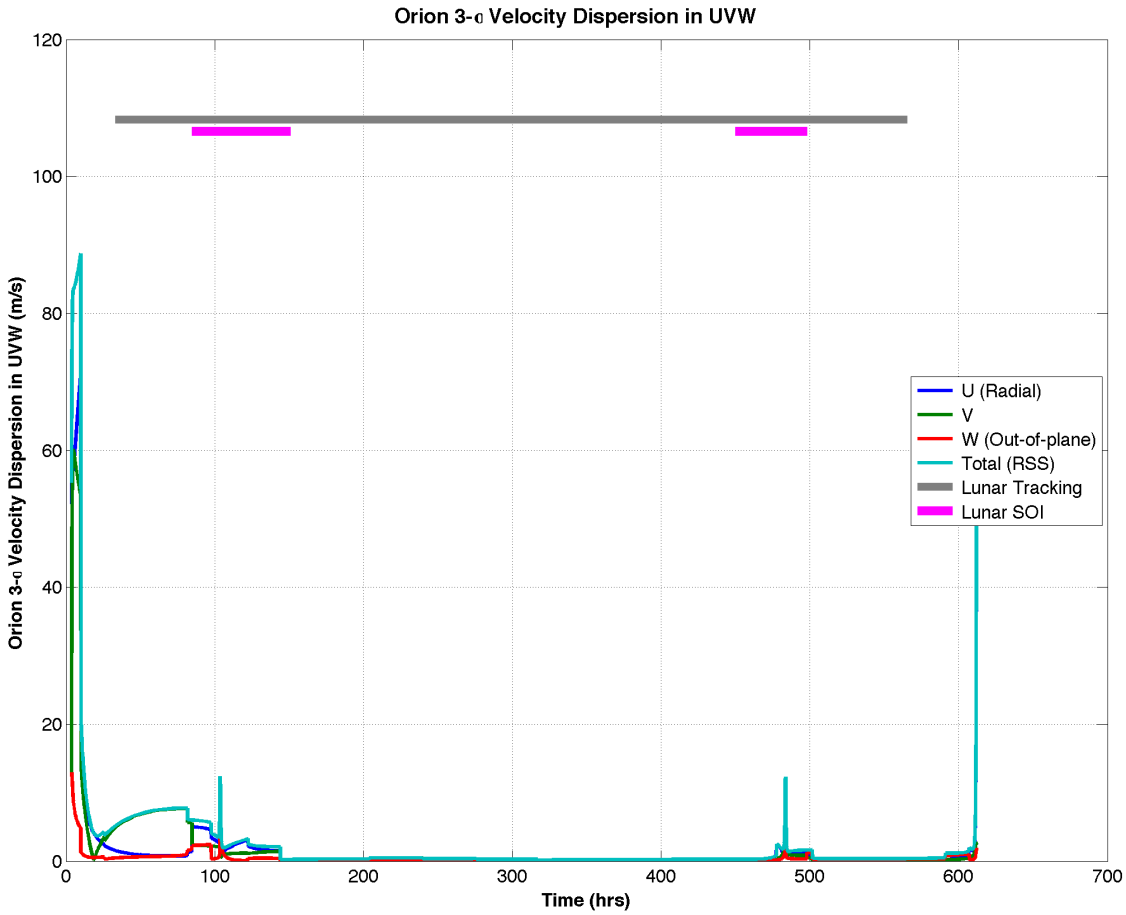

Figure 6. Velocity Trajectory Dispersions for the Entire Trajectory

Maneuver #	Type	t_{ig} (hrs)	$\|\Delta\mathbf{V}_{nom}\|$ (m/s)
1	OTC-1	9.81	0.000
2	OTC-2	25.81	0.000
3	OTC-3	81.60	0.000
4	OTC-4	97.60	0.000
5	OPF	103.60	174.537
6	OTC-5	122.41	0.000
7	OTC-6	144.00	0.000
8	DRI	169.21	243.072
9	OM-1	204.00	0.000
10	OM-2	240.00	0.000
11	OM-3	276.00	0.000
12	DRD	316.80	84.907
13	RTC-1	372.01	0.000
14	RTC-2	426.01	0.000
15	RTC-3	477.62	0.000
16	RPF	483.62	252.334
17	RTC-4	501.61	0.000
18	RTC-5	591.04	0.000
19	RTC-6	607.04	0.000
Total			**754.849**

Table 1. The Maneuver Plan

DRO-Orbit Phase

The navigation errors mapped to the time of the DRO Departure Maneuver are presented in Figures 11-12. The trajectory disperions mapped to the time of the DRO Departure Maneuver are presented in Figures 13-14.

STATISTICS FOR THE VARIATION IN THE TIME OF OTC-1

Table 7 contains the $|\Delta\mathbf{V}|$ statistics for when the time of OTC-1 is varied. Recall that the times in the table are MET, with TLI occuring at an MET of 3.81 hours, the nominal OCT-1 occurs at TLI + 6 hours.

Finally, Table 8 contains the delivery statistics at the EI point for each of these cases when the times of OTC-1 were varied.

STATISTICS FOR THE VARIATION IN TRANSLUNAR INJECTION (TLI) ACCURACY

Table 9 contains the values for the (TLI) injection errors and their error source.[5] One can see that the anticipated injection errors (from COVEAP (COVariance Error Analysis Program) are considerably larger than either the requirement or the case when INCA updates were used. One would expect that the $|\Delta\mathbf{V}|$ statistics would reflect this increase in error for the COVEAP errors.

Error	Value
U (Radial) Position	9443.9 m
V Position	59741.4 m
W (Out-of-Plane) Position	3347.3 m
U (Radial) Velocity	52.066 m/s
V Velocity	8.915 m/s
W (Out-of-Plane) Velocity	12.957 m/s

Table 2. Injection Accuracy (3σ)

Type	Value
Quiescent	3.531×10^{-9} $\mathrm{m}^2/\mathrm{s}^3$
Active (CM/SM)	1.310×10^{-5} $\mathrm{m}^2/\mathrm{s}^3$
Active (CM only)	7.877×10^{-5} $\mathrm{m}^2/\mathrm{s}^3$

Table 3. Vehicle Translation Process Noise Characteristics

Table 10 contains the $|\Delta\mathbf{V}|$ statistics for when the (TLI) injection errors were varied. As expected the COVEAP injection errors result in the largest $|\Delta\mathbf{V}|$ usage.

Finally, Table 11 contains the delivery statistics at the EI point for each of these cases when the injection errors were varied.

STATISTICS FOR THE VARIATION IN THE LENGTH OF OPTICAL NAVIGATION PASSES

Table 12 contains the $|\Delta\mathbf{V}|$ statistics for when length of the optical navigation passes is varied. The last column in the Table is the case when one hour passes are performed for all of the optical navigation passes except for the last two passes (before the RTC-5 and RTC-6). Rather surprisingly, there was no statistical difference in $|\Delta\mathbf{V}|$ usage when the length of the optical navigation passes was varied.

Finally, Table 13 contains the delivery statistics at the EI point for each of these cases when the length of the optical navigation pass was varied. As expected, the delivery accuracy improves with the length of the optical navigation pass.

CONCLUSIONS AND RECOMMENDATIONS

This paper has detailed the linear covariance analysis for the EM-1 DRO mission. The major contributor to the $|\Delta\mathbf{V}|$ usage is the TLI error; hence if the accuracy of TLI can be improved (to even meeting the requirements) there would be a substantial propellant savings. In addition, if the epoch of the first correction maneuver (OTC-1) were to occur at TLI + 3 hours, that would result in a substantial propellant savings. Finally, if the length of the optical navigation passes for the final two maneuvers (RTC-5 and RTC-6) were to be increased to 2 hours (from 1 hour), that would improve the trajectory dispersions at EI.

Parameter	Value
Field of View	20.0 degrees
Pixel Pitch	2.2 microns
Focal Length	16.0 mm
Focal Plane Array Size	2592 x 1944

Table 4. Optical Camera Characteristics

Error Type	Value
Centroid Measurement	0.14 (1σ) pixels
Diameter Measurement	0.14 (1σ) pixels
Centroid Measurement Markov IC	0.07 (1σ) pixels
Diameter Measurement Markov IC	0.07 (1σ) pixels
Misalignment Markov IC	15.0 (1σ) arc-seconds
Centroid Measurement Markov Time Constant	4.0 hrs
Misalignment Markov Time Constant	60.0 sec

Table 5. Optical Camera Error Model

Acknowledgements

Many thanks to Sara Scarritt for generating the measurement partials, to Dave Dannemiller for many discussions and suggestions, and to Greg Holt, and Dave Woffinden for many helpful discussions.

REFERENCES

[1] P. Maybeck, *Stochastic Models, Estimation and Control, Vol. 1*. New York, NY: Academic Press, 1979.

[2] C. D'Souza and R. Zanetti, "Navigation Design and Analysis for the Orion Earth-Moon Mission," *AAS/AIAA Space Flight Mechanics Conference*, February 2014.

[3] D. K. Geller, "Linear Covariance Techniques for Orbital Rendezvous Analysis and Autonomous Onboard Mission Planning," *Journal of Guidance, Navigation and Dynamics*, Vol. 29, No. 6, 2006, pp. 1404–1414.

[4] C. D'Souza and G. Holt, "Process Noise Assumptions for EM-1 for a 24-Jet Configuration," EG Technical Brief, FltDyn-CEV-13-49, Johnson Space Center, Engineering Directorate, Houston, TX, July 2013.

[5] United Launch Alliance, "ICPS Guidance & Navigation Findings and Results," *SIE CDR1 Kickoff Charts*, 3 2015, p. 256.

REFERENCES

[1] P. Maybeck, *Stochastic Models, Estimation and Control, Vol. 1*. New York, NY: Academic Press, 1979.

[2] C. D'Souza and R. Zanetti, "Navigation Design and Analysis for the Orion Earth-Moon Mission," *AAS/AIAA Space Flight Mechanics Conference*, February 2014.

[3] D. K. Geller, "Linear Covariance Techniques for Orbital Rendezvous Analysis and Autonomous Onboard Mission Planning," *Journal of Guidance, Navigation and Dynamics*, Vol. 29, No. 6, 2006, pp. 1404–1414.

Maneuver Execution Error	3σ Value
Noise (mm/s)	3.00
Bias (mm/s)	3.00
Scale Factor (ppm)	30.0
Misalignment (deg)	0.03

Table 6. The Maneuver Execution Error Model

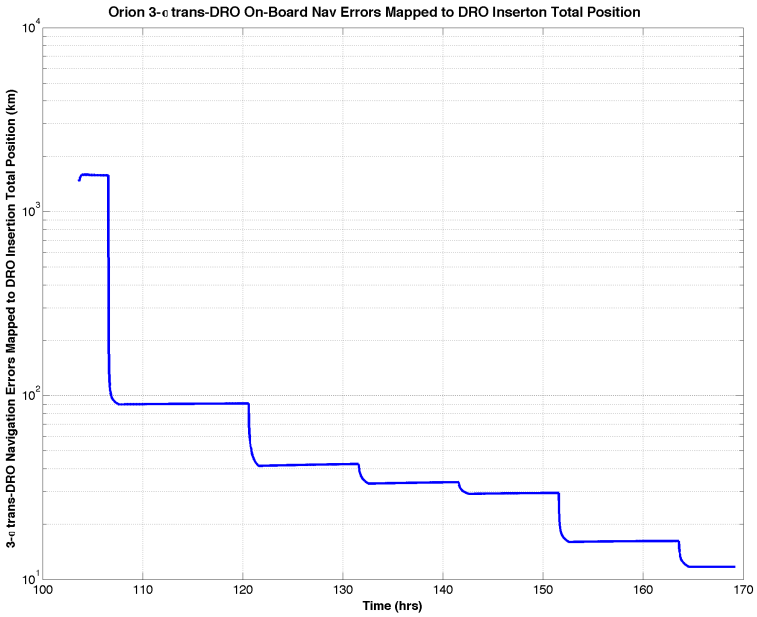

Figure 7. Trans-DRO Onboard Navigation Error Mapped to DRO Insertion Position Errors

[4] C. D'Souza and G. Holt, "Process Noise Assumptions for EM-1 for a 24-Jet Configuration," EG Technical Brief, FltDyn-CEV-13-49, Johnson Space Center, Engineering Directorate, Houston, TX, July 2013.

[5] United Launch Alliance, "ICPS Guidance & Navigation Findings and Results," *SIE CDR1 Kickoff Charts*, 3 2015, p. 256.

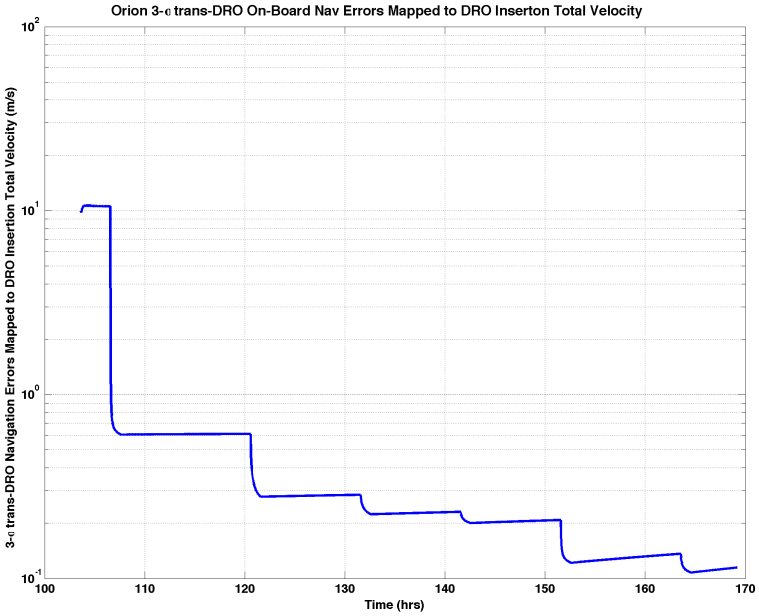

Figure 8. Trans-DRO Onboard Navigation Error Mapped to DRO Insertion Velocity Errors

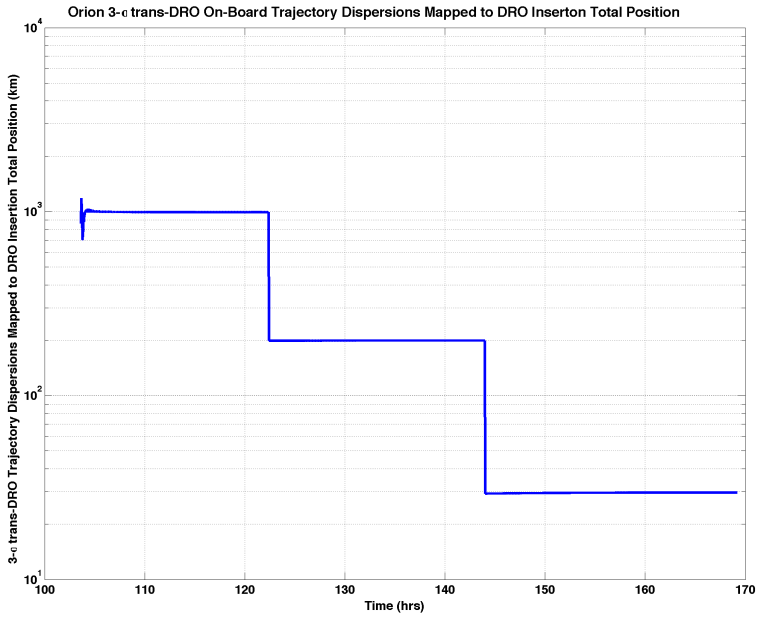

Figure 9. Trans-DRO Trajectory Dispersions Mapped to DRO Insertion Position Dispersions

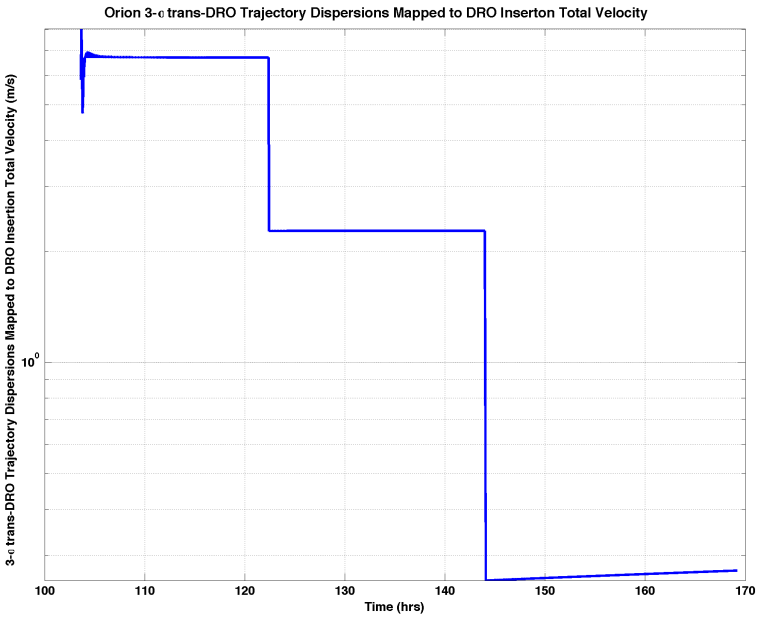

Figure 10. Trans-DRO Trajectory Dispersions Mapped to DRO Insertion Velocity Dispersions

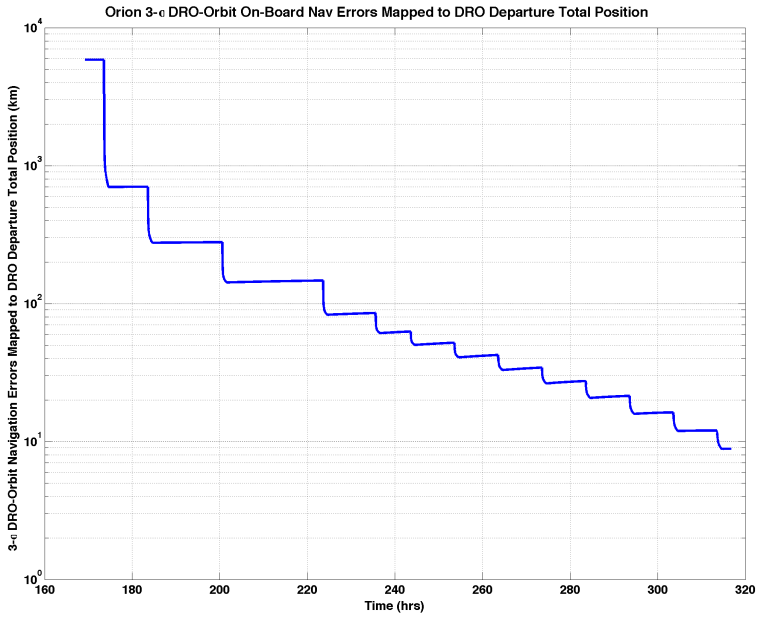

Figure 11. DRO Orbit Onboard Navigation Error Mapped to DRO Departure Position Error

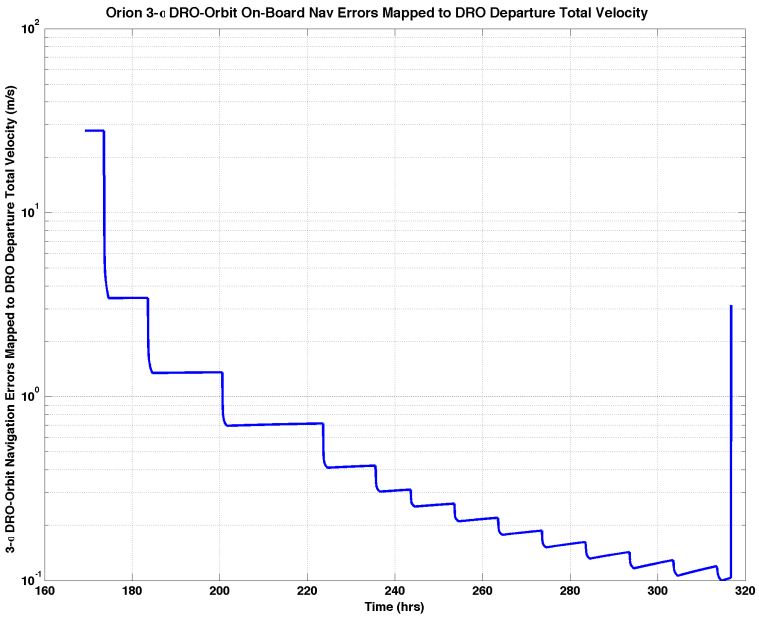

Figure 12. DRO Orbit Onboard Navigation Error Mapped to DRO Departure Velocity Error

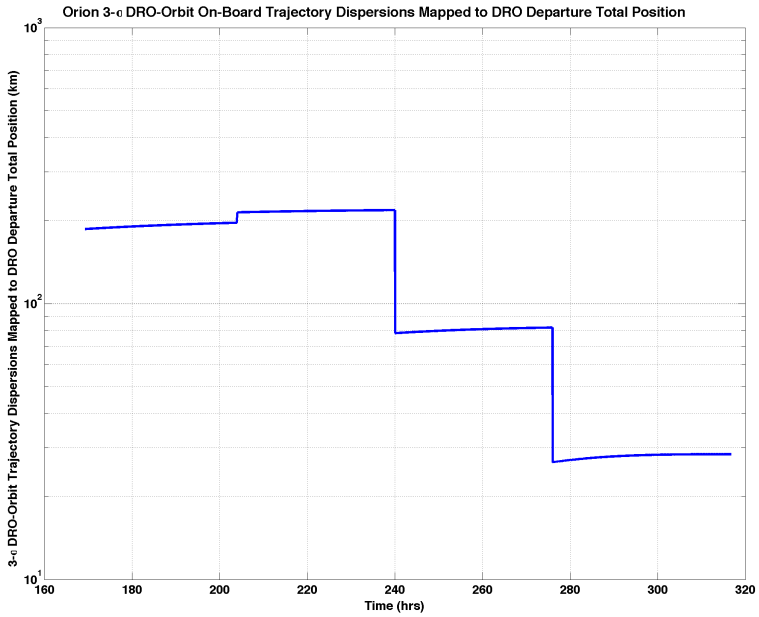

Figure 13. DRO Orbit Trajectory Dispersions Mapped to DRO Departure Position Dispersion

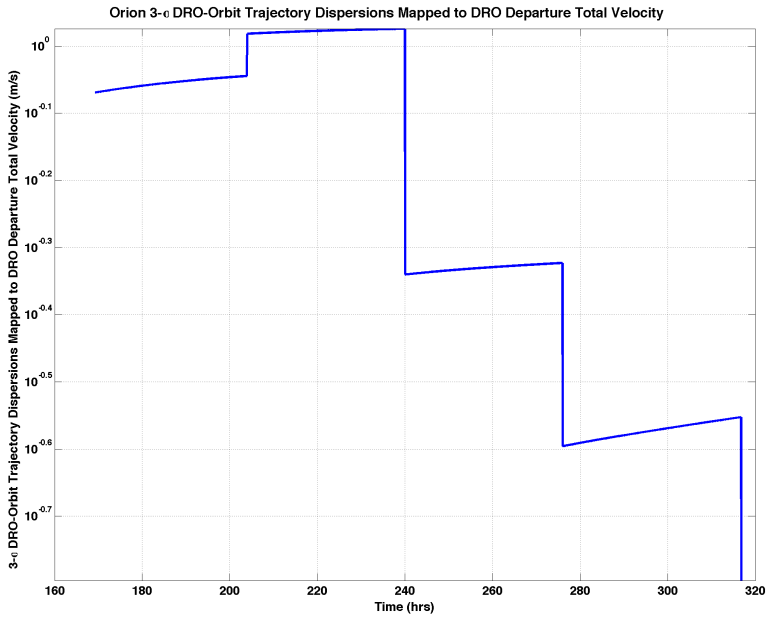

Figure 14. DRO Orbit Trajectory Dispersions Error Mapped to DRO Departure Velocity Dispersion

				OTC-1 at 3^{h}	OTC-1 at 4^{h}	OTC-1 at 5^{h}	OTC-1 at 6^{h}
Man #	Type	t_{ig} (hrs)	$\|\Delta\mathbf{V}\|_{nom}$ (m/s)	$\|\Delta\mathbf{V}\|_{99.73}$ (m/s)	$\|\Delta\mathbf{V}\|_{99.73}$ (m/s)	$\|\Delta\mathbf{V}\|_{99.73}$ (m/s)	$\|\Delta\mathbf{V}\|_{99.73}$ (m/s)
1	OTC-1	Varied	0.000	80.332	85.441	90.012	94.431
2	OTC-2	25.81	0.000	0.803	0.838	0.866	0.774
3	OTC-3	81.60	0.000	1.929	2.049	2.241	2.441
4	OTC-4	97.60	0.000	1.574	1.881	2.202	2.550
5	OPF	103.60	174.537	176.266	176.294	176.360	176.412
6	OTC-5	122.41	0.000	5.505	5.505	5.505	5.506
7	OTC-6	144.00	0.000	2.007	2.007	2.007	2.007
8	DRI	169.21	243.072	243.241	243.241	243.241	243.241
9	OM-1	204.00	0.000	0.590	0.590	0.590	0.590
10	OM-2	240.00	0.000	0.715	0.715	0.715	0.715
11	OM-3	276.00	0.000	0.475	0.475	0.475	0.475
12	DRD	316.80	84.907	85.097	85.097	85.097	85.097
13	RTC-1	372.01	0.000	0.349	0.349	0.349	0.349
14	RTC-2	426.01	0.000	0.374	0.374	0.374	0.374
15	RTC-3	477.62	0.000	3.318	3.318	3.318	3.318
16	RPF	483.62	252.334	252.678	252.678	252.678	252.678
17	RTC-4	501.61	0.000	1.664	1.664	1.664	1.664
18	RTC-5	591.04	0.000	1.232	1.232	1.232	1.232
19	RTC-6	607.04	0.000	2.659	2.659	2.659	2.659
Total			**754.849**	**860.807**	**866.406**	**871.585**	**876.513**

Table 7. $|\Delta\mathrm{V}|$ Statistics for the Variation in the Times of OTC-1

EI Delivery Error	OTC-1 at 3^{h}	OTC-1 at 4^{h}	OTC-1 at 5^{h}	OTC-1 at 6^{h}
Latitude (3σ)	0.559 °	0.559 °	0.559 °	0.559 °
Longitude (3σ)	0.022 °	0.022 °	0.022 °	0.022 °
Flight Path Angle (3σ)	0.256 °	0.256 °	0.256 °	0.256 °
Heading Angle (3σ)	0.303 °	0.303 °	0.303 °	0.303 °

Table 8. The Final Entry Interface 3σ Delivery Statistics as a Function of the Time of OTC-1

Error	COVEAP	Requirement	w INCA Updates
U (Radial) Position	9443.9 m	7950.5 m	6412.9 m
V Position	59741.4 m	41301.6 m	41301.6 m
W (Out-of-Plane) Position	3347.3 m	4696.0 m	2149.1 m
U (Radial) Velocity	52.066 m/s	37.033 m/s	36.850 m/s
V Velocity	8.915 m/s	6.437 m/s	6.282 m/s
W (Out-of-Plane) Velocity	12.957 m/s	8.458 m/s	8.102 m/s

Table 9. Variation in Injection Accuracy (3σ)

				COVEAP	Requirement	w INCA Updates
Man #	Type	t_{ig} (hrs)	$\|\Delta\mathbf{V}\|_{nom}$ (m/s)	$\|\Delta\mathbf{V}\|_{99.73}$ (m/s)	$\|\Delta\mathbf{V}\|_{99.73}$ (m/s)	$\|\Delta\mathbf{V}\|_{99.73}$ (m/s)
1	OTC-1	9.81	0.000	94.431	68.466	66.551
2	OTC-2	25.81	0.000	0.774	0.619	0.611
3	OTC-3	81.60	0.000	2.441	2.054	2.041
4	OTC-4	97.60	0.000	2.550	1.890	1.858
5	OPF	103.60	174.537	176.412	176.283	176.275
6	OTC-5	122.41	0.000	5.506	5.505	5.505
7	OTC-6	144.00	0.000	2.007	2.007	2.007
8	DRI	169.21	243.072	243.241	243.241	243.241
9	OM-1	204.00	0.000	0.590	0.590	0.590
10	OM-2	240.00	0.000	0.715	0.715	0.715
11	OM-3	276.00	0.000	0.475	0.475	0.475
12	DRD	316.80	84.907	85.097	85.097	85.097
13	RTC-1	372.01	0.000	0.349	0.349	0.349
14	RTC-2	426.01	0.000	0.374	0.374	0.374
15	RTC-3	477.62	0.000	3.318	3.318	3.318
16	RPF	483.62	252.334	252.678	252.678	252.678
17	RTC-4	501.61	0.000	1.664	1.664	1.664
18	RTC-5	591.04	0.000	1.232	1.232	1.232
19	RTC-6	607.04	0.000	2.659	2.659	2.659
Total			**754.849**	**876.513**	**849.216**	**847.240**

Table 10. $|\Delta\mathbf{V}|$ Statistics for the Variation in (TLI) Injection Errors

EI Delivery Error	COVEAP	Requirement	w INCA Updates
Latitude (3σ)	0.559 °	0.559 °	0.559 °
Longitude (3σ)	0.022 °	0.022 °	0.022 °
Flight Path Angle (3σ)	0.256 °	0.256 °	0.256 °
Heading Angle (3σ)	0.303 °	0.303 °	0.303 °

Table 11. The Final Entry Interface 3σ Delivery Statistics as a Function of the Injection Accuracy

				1 Hour Pass	1.5 Hour Pass	2 Hour Pass	1^* Hour Pass
Man #	Type	t_{ig} (hrs)	$\|\Delta\mathrm{V}\|_{nom}$ (m/s)	$\|\Delta\mathbf{V}\|_{99.73}$ (m/s)	$\|\Delta\mathbf{V}\|_{99.73}$ (m/s)	$\|\Delta\mathbf{V}\|_{99.73}$ (m/s)	$\|\Delta\mathbf{V}\|_{99.73}$ (m/s)
1	OTC-1	9.81	0.000	94.431	94.431	94.431	94.431
2	OTC-2	25.81	0.000	0.774	0.775	0.775	0.774
3	OTC-3	81.60	0.000	2.441	2.435	2.429	2.441
4	OTC-4	97.60	0.000	2.550	2.550	2.550	2.550
5	OPF	103.60	174.537	176.412	176.381	176.362	176.412
6	OTC-5	122.41	0.000	5.506	5.401	5.385	5.506
7	OTC-6	144.00	0.000	2.007	1.963	1.953	2.007
8	DRI	169.21	243.072	243.241	243.225	243.216	243.241
9	OM-1	204.00	0.000	0.590	0.570	0.553	0.590
10	OM-2	240.00	0.000	0.715	0.677	0.647	0.715
11	OM-3	276.00	0.000	0.475	0.456	0.441	0.475
12	DRD	316.80	84.907	85.097	85.092	85.088	85.097
13	RTC-1	372.01	0.000	0.349	0.337	0.329	0.349
14	RTC-2	426.01	0.000	0.374	0.360	0.350	0.374
15	RTC-3	477.62	0.000	3.318	3.239	3.173	3.318
16	RPF	483.62	252.334	252.678	252.664	252.655	252.678
17	RTC-4	501.61	0.000	1.664	1.599	1.573	1.664
18	RTC-5	591.04	0.000	1.232	1.165	1.125	1.232
19	RTC-6	607.04	0.000	2.659	2.436	2.322	2.780
Total			**754.849**	**876.513**	**875.755**	**875.357**	**876.634**

Table 12. ΔV Statistics for the Variation in the Length of the Optical Navigation Pass

EI Delivery Error	1 Hour Pass	1.5 Hour Pass	2 Hour Pass	1^* Hour Pass
Latitude (3σ)	0.559 °	0.488 °	0.424 °	0.438 °
Longitude (3σ)	0.022 °	0.019 °	0.018 °	0.018 °
Flight Path Angle (3σ)	0.256 °	0.223 °	0.194 °	0.200 °
Heading Angle (3σ)	0.303 °	0.265 °	0.231 °	0.239 °

Table 13. The Final Entry Interface 3σ Delivery Statistics as a Function of the Length of the Optical Navigation Pass